SiO_2 glass density to lower-mantle pressures

Sylvain Petitgirard [a*], Wim J. Malfait [b], Baptiste Journaux [c], Ines E. Collings [d,f], Eleanor S. Jennings [a], Ingrid Blanchard [a], Innokenty Kantor [e], Alexander Kurnosov [a], Marine Cotte [f,g], Thomas Dane [f], Manfred Burghammer [f,h] , and David C. Rubie [a]

[a] *Bayerisches Geoinstitut, University of Bayreuth, Bayreuth, D-95440, Germany*

[b] *Laboratory for Building Energy Materials and Components, Swiss Federal Laboratories for Materials Science and Technology, Empa, 8600 Dübendorf, Switzerland*

[c] *Université Grenoble Alpes, Laboratoire de Glaciologie et Géophysique de l'Environnement (LGGE), Grenoble, France*

[d] *Laboratory of Crystallography, University of Bayreuth, Bayreuth, D-95440, Germany*

[e] *Danmarks Tekniske Universitet, Lyngby, Denmark*

[f] *European Synchrotron Radiation Facility, BP 220, Grenoble F-38043, France*

[g] *Sorbonne Universités, UPMC Univ Paris 06, CNRS, UMR 8220, Laboratoire d'archéologie moléculaire et structurale (LAMS), 4 Place Jussieu 75005 Paris, France*

[h] *Department of Analytical Chemistry, Ghent University, B-9000 Ghent, Belgium*

* Corresponding author: Sylvain.Petitgirard@uni-bayreuth.de

/Abstract/

The convection or settling of matter in the deep Earth's interior is mostly constrained by density variations between the different reservoirs. Knowledge of the density contrast between solid and molten silicates is thus of prime importance to understand and model the dynamic behaviour of the past and present Earth. SiO_2 is the main constituent of the Earth's mantle and is the reference model system for the behaviour of silicate melts at high pressure. Here, we apply our recently developed X-ray absorption technique to the density of SiO_2 glass up to 110 GPa, doubling the pressure range for such measurements. Our density data validate recent molecular dynamics (MD) simulations and are in good agreement with previous experimental studies conducted at lower pressure. Silica glass rapidly densifies up to 40 GPa, but the density trend then flattens to become asymptotic to the density of SiO_2 minerals above 60 GPa. The density data present two discontinuities at ~17 and ~60 GPa that can be related to a silicon coordination increase from 4 to a mixed 5/6 coordination and from 5/6 to 6-fold, respectively. SiO_2 glass becomes denser than $MgSiO_3$ glass at ~40 GPa, and its density becomes identical to that of $MgSiO_3$ glass above 80 GPa. Our results on SiO_2 glass may suggest that a variation of SiO_2 content in a basaltic or pyrolitic melt with pressure has at most a minor effect on the final melt density, and iron partitioning between the melts and residual solids is the predominant factor that controls melt buoyancy in the lowermost mantle.

/body/

The concentration of SiO_2 exceeds 45 mole per cent in the Earth's mantle [1], and has a primary role in the properties of minerals and melts at mantle conditions. The SiO_2 reference system is therefore of great importance for constraining the density, compressibility, and atomic coordination changes of the more complex silicate melt compositions that can be found in the deep interior of the Earth and other rocky planets [2,3]. Studies of the high-pressure (>25 GPa) properties of simple silicate

melts, with e.g. MgO, SiO_2 and Al_2O_3, are scarce, because of high melting temperatures [4,5], also because of their insulating character (high-band gap) that prohibits the use of the standard YAG laser-heating system in diamond anvil cell (DAC). In addition, glasses and melts made of light elements (with low atomic mass) produce a weak X-ray scattering signal that is difficult to extract from the background of the diamond anvils. In contrast, the X-ray absorption method enables the study of melts [6,7] and glasses [8] composed of light elements, because it retains its sensitivity also for light elements, and the data interpretation is straightforward.

Generating high pressure and temperature conditions limit the accuracy and diversity of analytical techniques for in situ melt studies. Investigations on glasses as melt proxies can circumvent these limitations, but it is important to account for differences between glasses and melts and their comparison requires some caution. In the liquid state, structural equilibration is faster than the external perturbations, and the properties of the melt rapidly relax to new pressure or temperature conditions [9,10]. During cooling of the melt, the rate of equilibration slows down and, assuming crystallization is avoided, the structure is frozen at the glass transition [11]. The divide between the liquid and glassy state depends not only on temperature, but also on the frequency of the probe. Ultrasonic measurements of high temperature melts can sample both the elastic and configurational compressibility [12,13], but Brillouin scattering only probes the elastic compressibility [14]. Cold compression experiments on glasses represent an intermediate case: although the structure and properties are not in equilibrium, significant configurational changes undoubtedly take place upon compression to lower mantle pressure [8,15,16] and strong similarities exist between the structure of a high pressure glass and melt, most notably with respect to Si coordination [2,8,15–18].

At ambient pressure, SiO_2 glass has a fully polymerized structure, with silicon atoms coordinated with four oxygen atoms to form corner-sharing SiO_4 tetrahedrons. The structure contains nominally no non-bridging oxygens (NBO) per tetrahedron (T) (NBO/T=0), meaning that each oxygen atom connects two silicon atoms forming a network of silica tetrahedra. The incorporation of network modifiers, such as magnesium oxide, increases the number of non-bridging oxygens per tetrahedron, e.g. nominal NBO/T=2 for $MgSiO_3$. Note that the concept of NBO/T breaks down at high pressure once Si increases its coordination at the expense of NBO, i.e. NBO decreases and T decreases. At ambient pressure, SiO_2 glass density is lower than expected from the atomic weights of its constituents, because of a relatively open structure [19–21]. Although brittle at a macroscopic scale at ambient conditions, SiO_2 glass can deform elastically and reversibly up to 9 GPa [22]. Above this elastic yield pressure, the recovered pressurised glass shows signs of a permanent densification through plastic deformation [23–26], which saturates at about 25 GPa [22,27]. The in situ density of SiO_2 glass under compression follows a steep, approximately linear trend up to 35-40 GPa, but the rate of densification becomes less steep at higher pressures [8,28]. Under large pressure gradients, SiO_2 glass shows variable strength related to changes of coordination and/or degree of depolymerisation [29].

Understanding the properties of the fully polymerized SiO_2 network with pressure is essential to simulate and predict the role and influence of cation network modifiers in high-pressure melts of the deep Earth. Here we measured the density of pure SiO_2 glass up to 110 GPa using the X-ray absorption method adapted to the environment of the DAC [30] and use the glass data to estimate the density of the corresponding melts. Our results show that the density of SiO_2 and $MgSiO_3$ glass and melt are very similar at high pressure and we conclude that the main factor controlling melt

buoyancy in the lowermost mantle is the partitioning of iron between the melt and coexisting mineral phases, with at most a minor role for the silica content of the melt.

X-ray absorption measurements were performed on the of the ID13 (nano-branch) and on the ID21 (side-branch) [31] beamlines at the European Synchrotron Radiation Facility (ESRF, Grenoble, France) (Fig S1A-C). Samples were loaded in BX90 DAC [32] and pressure determined from the shift of the ruby fluorescence [33] or diamond line [34] (details in the supplementary file). The measurement procedure is the same as for $MgSiO_3$ glass [30] with 2D-mapping of the sample under two orientations: i) through the diamond to obtain the path length (x) of the X-rays through the SiO_2 sample (Fig. 1A-B and Fig. S2A-B) and ii) through the Be gasket in order to measure the X-ray attenuation (I/I_0) of SiO_2 glass under pressure (Fig. 1C-D and Fig. S2C-D). The edges of the sample, defining the path length (x), can be obtained with a precision better than 1 μm, corresponding to uncertainty of about 2% on the density. The absorbance (μ_{HP}) of the sample was extracted from the correlation between the X-ray attenuation and the path length of the sample obtained from both maps (Fig. 1E and Fig. S2E). The slope of the linear regression gives the linear absorbance at high pressure (μ_{HP}) through the Beer-Lambert relation:

$$\ln(I/I_0) = -\mu_{HP} . x \quad (1)$$

The density at high pressure (ρ_{HP}) was then calculated by:

$$\rho_{HP} / \mu_{HP} = \rho_0 / \mu_0 \quad (2)$$

The attenuation coefficient at ambient pressure (μ_0) was determined from the absorption of a double-polished plate of SiO_2 using the same set-up on the beamline, and the ambient pressure density (ρ_0) of Suprasil silica glass is 2.203 ± 0.008 g/cm^3. Our density measurements on SiO_2 glass were performed between 2 and 110 GPa,

doubling the former pressure range [8] (Fig. 2A). Our data are in good agreement with previous experimental results [8,28], as well as with densities predicted from *ab-initio* MD calculations (Fig. 2A) [18]. The density of SiO_2 glass can be separated in three pressure regimes based on different compressibility trends, as evidenced by the f-F plot (Fig. 2B) in the Vinet form [35]. Although it is less evident when using the eulerian definition [36] (Fig. S3), two domains are also visible. First, we identify a steep and quasi-linear increase in density up to ~17 GPa, followed by a curvature of the trend between 17 and 60 GPa with a decrease of the compressibility as a function of pressure, and finally, a flattening and asymptotic trend to the density of the SiO_2 stishovite and the $CaCl_2$ phases [37,38] above 60 GPa (Fig. 2A). The dataset cannot be described by a single equation-of-state (EoS), third or fourth order Birch-Murnghan (BM) (SI, Fig. S4A-B). Instead, the three domains identified in the pressure-density data and f-F plot (Fig. 2A-B) suggest that distinct compression mechanisms are dominant for the different pressure domains, related the Si coordination. Our interpretation is based on MD simulations [18] that show almost exclusively $^{[4]}$Si below ~17 GPa, a rapid decrease of $^{[4]}$Si starting around ~20 GPa, $^{[5]}$Si as the dominant species mixed with $^{[6]}$Si between 20 and 60 GPa, and the abrupt near disappearance of $^{[5]}$Si in favour of $^{[6]}$Si at ~60 GPa and no further major structural changes up to ~140 GPa [39]. The lack of long-range order and multiple coordination lead to gradual structural transition explaining the lack of abrupt changes in the compression curve (Fig. 2A). The pressure ranges for the different species are in very good agreements with our data and provide a framework to explain the density and compressibility trends in SiO_2 glass, but further investigations are required. Interestingly, the compression curve for $MgSiO_3$ glass does not display the distinct pressure domains observed for SiO_2 glass, and a single equation of state (EoS) can be

used from 0 to 130 GPa [30]. The depolymerized nature of $MgSiO_3$ glass may allow the structure to approach quasi-equilibrium densities, i.e. more melt-like configurations, upon compression, whereas the highly polymerized SiO_2 structure involves crossing higher potential energy barriers. This is supported by the existence of much larger irreversible densifications for SiO_2 glass [26] compared to $MgSiO_3$ glass [40] and consistent with the role of non-bridging oxygens in facilitating Si coordination increases [41]. For the high pressure regime (P>60 GPa) where Si coordination changes are absent [8,18,39,42], or minor [43], configurational contributions to the compressibility for both glass and melt is expected to be minimal, and above this pressure, SiO_2 melt may behave in a similar way as the glass.

Common EoS such as the Birch-Murnaghan or Vinet EoS are of limited theoretical validity for glasses and melts, where densification occurs in large part through configurational changes. However, they can provide an empirical means to interpolate between data but extrapolations far beyond the experimental data should be avoided. Given the occurrence of distinct pressure domains (Fig. 2A-B), a fit with a single EoS for the entire pressure range is not appropriate (SI, Fig. S4). The f-F_V plot identified a distinct regime above ~60 GPa (Fig. 2B), where the coordination of Si remains constant ($^{[6]}$Si) [18] and close densities to that of the crystalline SiO_2 phases, suggesting a single compression mechanism above 60 GPa. The positive and linear slope in both f-F plots (Fig. 2B and SI, Fig. S3) indicates that a third order BM EoS with a K'_T>4 is appropriate. We used 3rd order BM EoS fits with bulk modulus derivatives ($K'_{HP,T0}$) fixed at 4, 5 and 6, named HP1, HP2 and HP3 (Table S2 and Fig. 2C). Fixing $K'_{HP1,T0}$ at 4 results in a high bulk modulus ($K_{HP1,T0}$ = 244.7 GPa) and a density $\rho_{HP1,0}$ = 4.05 g.cm^{-3}. When $K'_{HP2,T0}$ is fixed at 5 or 6, $K_{HP2,T0}$ decreases to = 183.3

and 138 GPa, with $\rho_{HP2,0}$ = 3.95 and 3.85 g/cm^3, respectively. The different values for the EoS are quite similar to previous estimates [8], but are now more robust as we used a larger pressure range. The differences between the EoS for different $K'_{HP,T0}$ reside mostly in ρ_0, with minimal variations upon extrapolation to higher pressures (Fig. 2C). In the discussion below, we use the values of HP2 EoS (Table S2).

For the low-pressure (<60 GPa), the scattering of the points in the f-F plot using the eulerian definition with a negative slope (SI, Fig. S3) suggest that a classical EoS might not be appropriate. Indeed, a 4th order BM EoS with ρ_0 = 2.200 g.cm^{-3}, K_{T0} = 27.6 ± 3.2 GPa, K'_{T0} = 1.95 ± 0.52 and K''_{T0} = -0.098 ± 0.021 GPa^{-1} reproduces the data, but the values for K'_{T0} and K''_{T0} are not realistic. The low pressure data may be further split in two domains as suggested by the f-F_V plot in Fig. 2B, but we have opted to use a 2nd order polynomial function as proposed elsewhere for data not satisfying the Birch's law [44], with :

$$\rho = -0.00053802\ (\pm 94)\ P^2 + 0.076204\ (\pm 42)\ P + 2.203 \quad (3)$$

where ρ is expressed in g/cm^3 and P in GPa (Fig. S5). The difficulty to fit a classical EoS arises from the occurrence of multiple densification mechanisms, with topological changes below ~17 GPa and an increase in Si coordination with mixed Si coordination at higher pressure [18]. The fact that the starting SiO_2 glass is a two-phase mixture, with a High-Density Amorphous (HDA) and Low-Density Amorphous (LDA) phase [45], may further complicate the use of a classical EoS. However, we cannot rule out that the melt will be composed of a single phase in the low-pressure regime, and it can reach an equilibrated structure below 60 GPa.

The experimentally determined density of SiO_2 glass crosses over with that of $MgSiO_3$ counterpart at about 40 GPa (Fig. 2C). The densities of both compositions converge at higher pressure, above ~90 GPa (Fig. 2C, Fig. 3), and remain nearly equal at all higher pressure studied here and probably up to core-mantle boundary (CMB) pressure following our extrapolation (Fig. 2C, Fig. 3). From our EoS at 300 K for SiO_2 for the deep mantle (P>60 GPa), we calculated densities along an isotherm at 4000 K (Fig. 3) using the thermal expansion coefficients from *ab-initio* MD simulations [5]. The density difference between the SiO_2 and $MgSiO_3$ high-temperature isotherms at 4000 K is slightly larger than at room temperature, with a density difference of ~ 4.0 % at 60 GPa that decreases to ~ 1.3 % at 140 GPa (Fig. 3), although the thermal expansion can have some uncertainties too [46] (Fig. 3). This larger difference at high temperature results from different thermal expansivities for the two compositions and is in good agreement with *ab-initio* calculations, that also found a higher density for SiO_2 compared to $MgSiO_3$ at high temperature [47]. Whereas SiO_2 is the archetypal light component in silicate melts at crustal and upper mantle conditions and is responsible for the low density of granitic and other felsic melts, it is a more a neutral to a dense component to the buoyancy of silicate melts in the lower parts of the mantle.

For the pressure conditions of the deep mantle (>90 GPa), the near identical densities of SiO_2 and $MgSiO_3$ melts suggest that SiO_2 enrichment or depletion in the melt compared to the mineral phases will play a minor role in the final density evolution. It is expected that the SiO_2 content of the melt will evolve with pressure in the lower mantle: the SiO_2 content of the eutectic composition of a basaltic melt would rise from 64 % at 26 GPa up to 70 % at the CMB [48] while the SiO_2 content of a pyrolitic

melt would decrease from 43 % down to 40 % for similar pressure [49]. However such variations in the SiO_2 fraction should at most have a minor effect on the final melt density. Secondly, because of the very small density contrast between iron-free compositions and their counterpart solid phases (Fig. 2C and Fig. 3), the buoyancy of melts in the deep Earth will be mainly influenced by the addition of iron as the main heavy element. At the core-mantle boundary today, the density difference between the PREM-model [50] and the iron-free melts is about 5% (Fig. 3). In order for a silicate melt to be denser than the PREM-model and buoyantly stable at the CMB today, the iron oxide content should be at least 25 mol%, based on the density of $MgSiO_{3\ [30]}$ and FeO [47] for a melt at 4000 K. In the early Earth, the lower mantle must have been at a higher temperature, and both the solids and melts were at relatively similar temperatures. Thus, the density difference between the solid and the melt would have been less than it is today. Because iron is a less compatible element, it concentrates in the melts. Although the K_D $([Fe^{sol}]/[Mg^{sol}])/([Fe^{melt}]/[Mg^{melt}])$ value remains debated [51,52], the amount of iron in the melt, given by the partitioning of Fe ($D_{Fe} = [Fe^{sol}]/([Fe^{melt}]$), will be at least 50% [52] higher than in the solids. Therefore, the buoyancy of melts mainly depends on P, T, X_{FeO} and K_D values. At CMB conditions, a melt will be stable for a bulk FeO > 10% for any partitioning value measured experimentally [51–53] (Fig. S6). However for lower FeO content, lower K_D values are required and would considerably restrict the amount of melt present at the CMB. Thus, a basal magma ocean may have formed, but it strongly depends on the iron partitioning, the amount of FeO available and its persistence through time also remains an open question.

In conclusion, our density data on SiO_2 confirm the previous reported densities [8] as well as MD simulations [18]. As observed previously for $MgSiO_3$ [30], amorphous SiO_2 becomes nearly as dense, within a few per cent, as the coexisting crystalline phases for pressures above 60 GPa. At pressures of the lower mantle (>80 GPa), the densities of SiO_2 and $MgSiO_3$ glasses are the same and at high temperature, the SiO_2 melts is only slightly denser, within two to four per cent. Thus, variation of few per cent of the SiO_2 fraction in the melt composition [48,49] will have a minor effect on the final density of the melt at high pressure. The main parameter that controls the buoyancy of lower mantle melts is the iron content of the melt in comparison to that of the coexisting solids. Even a small excess of iron in the melt compared to the solids will lead to a density crossover and the accumulation of silicate melt on top of the core during the early Earth's formation [54]. These trapped melts, or their Fe-rich crystallization products, may explain large low-shear-velocity provinces (LLSVPs) and ultra low velocity zones (ULVZs) above the CMB as detected today by seismic tomography and constitute ideal candidates for pristine geochemical reservoirs in the deep mantle [55].

Acknowledgments

We are particularly grateful to H. Shultz for the polishing of the starting samples prior to the beamtime. We are thankful to M. Hanfland for the access and use of the off-line Raman system of beamline ID09. S.P. is grateful to S. Pascarelli and R. Torchio for the loan of the portable ruby system of beamline ID24. D. Bugnazet and M. Salomé are thanked for their help in designing the sample holder for ID21 measurements. We acknowledge the ESRF for provision of beamtime under the proposal ES-354 and ES-590. The two anonymous reviewers are also acknowledged for their fruitful

comments. S.P. is financed by a DFG grant (PE 2334/1-1). S.P. and D.C.R are supported by the European Research Council (ERC) Advanced Grant "ACCRETE" (contract number 290568).

References

[1] W. F. McDonough and S. S. Sun, Chem. Geol. **120**, 223 (1995).

[2] C. Sanloup, J. W. . Drewitt, Z. Konopkova, P. Dalladay-Simpson, D. M. Morton, N. Rai, W. VanWestrenen, and W. Morgenroth, Nature **503**, 104 (2013).

[3] M. Millot, N. Dubrovinskaia, A. Cernok, S. Blaha, L. Dubrovinsky, D. G. Braun, P. M. Celliers, G. W. Collins, J. H. Eggert, and R. Jeanloz, Science. **347**, 418 (2015).

[4] A. Zerr and R. Boehler, Nature **371**, 506 (1994).

[5] N. de Koker and L. Stixrude, Geophys. J. Int. **178**, 162 (2009).

[6] W. J. Malfait, R. Seifert, S. Petitgirard, J.-P. Perrillat, M. Mezouar, T. Ota, E. Nakamura, P. Lerch, and C. Sanchez-Valle, Nat. Geosci **7**, 122 (2014).

[7] R. Seifert, W. J. Malfait, S. Petitgirard, and C. Sanchez-Valle, Earth Planet. Sc. Lett. **381**, 12 (2013).

[8] T. Sato and N. Funamori, Phys. Rev. Lett. **101**, 209604 (2008).

[9] I. Farnan and J. F. Stebbins, Science. **265**, 1206 (1994).

[10] W. J. Malfait and W. E. Halter, Phys. Rev. B **77,** 014201 (2008).

[11] C. T. Moyhihan, A. J. Easteal, J. Wilder, and J. Tucker, J. Phys. Chem. **78**, 2673 (1974).

[12] M. L. Rivers and I. S. E. Carmichael, J. Geophys. Res. **92**, 9247 (1987).

[13] R. L. Lange and I. S. . Carmichael, Rev. Min. **24**, 25 (1990).

[14] A. Polian, D. Vo-Thanh, and P. Richet, Eur. Lett. **57**, 375 (2002).

[15] C. Meade, R. J. Hemley, and H. K. Mao, Phys. Rev. Lett. **69**, 1387 (1992).

[16] C. J. Benmore, E. Soignard, S. A. Amin, M. Guthrie, S. D. Shastri, P. L. Lee, and J. L. Jarger, Phys. Rev. B **81**, 054105 (2010).

[17] B. B. Karki, D. Bhattarai, and L. Stixrude, Phys. Rev. B **76**, 245504 (2007).

[18] M. Wu, Y. Liang, J.-Z. Jiang, and J. S. Tse, Sci. Rep. **2**, 398 (2012).

[19] G. Y. Shen, Q. Mei, V. B. Prakapenka, P. Lazor, S. Sinogeikin, Y. Meng, and C. Park, Proc. Natl. Acad. Sci. USA **108**, 6004 (2011).

[20] T. Sato, N. Funamori, and T. Yagi, Nat. Comm. **2**,345 (2011).

[21] C. Weigel, A. Polian, M. Kint, B. Ruffle, M. Foret, and R. Vacher, Phys. Rev. Let. **109**, 245504 (2012).

[22] T. Deschamps, A. Kassir-Bodon, C. Sonneville, J. Margueritat, C. Martinet, D. de Ligny, A. Mermet, and B. Champagnon, J. Phys. Condens. Matter **25**, 025402 (2013).

[23] P. W. Bridgman and I. Simon, J. Appl. Phys. **24**, 405 (1953).

[24] J. D. Mackenzie and R. P. Laforce, Nature **197**, 480 (1963).

[25] S. Sugai and A. Onodera, Phys. Rev. Lett. **77**, 4210 (1996).

[26] B. Champagnon, C. Martinet, M. Boudeulle, D. Vouagner, C. Coussa, T. Deschamps, and L. Grosvalet, J. Non-Cryst. Solids **354**, 569 (2008).

[27] T. Deschamps, J. Margueritat, C. Martinet, A. Mermet, and B. Champagnon, Sci. Rep. **4**, 7193 (2014).

[28] C. Meade and R. Jeanloz, Phys. Rev. B **35**, 236 (1987).

[29] C. Meade and R. Jeanloz, Science. **241**, 1072 (1988).

[30] S. Petitgirard, W. J. Malfait, R. Sinmyo, I. Kupenko, L. Hennet, D. Harries, T. Dane, M. Burghammer, and D. C. Rubie, Proc. Natl. Acad. Sci. USA **112**, 14186 (2015).

[31] M. Cotte, E. Pouyet, M. Salome, C. Rivard, W. De Nolf, H. Castillo-Michel, T. Fabris, L. Monico, K. Janssens, T. Wang, P. Sciau, L. Verger, L. Cormier, O. Dargaud, E. Brun, D. Bugnazet, B. Fayard, B. Hesse, A. E. P. del Real, G. Veronesi, J. Langlois, N. Balcar, Y. Vandenberghe, V. A. Sole, J. Kieffer, R. Barrett, C. Cohen, C. Cornu, R. Baker, E. Gagliardini, E. Papillon, and J. Susini, J. Anal. Atom. Spectrom. **32**, 477 (2017).

[32] I. Kantor, V. Prakapenka, A. Kantor, P. Dera, A. Kurnosov, S. Sinogeikin, N. Dubrovinskaia, and L. Dubrovinsky, Rev. Sci. Instrum. **83**, 125102 (2012).

[33] H. K. Mao, J. Xu, and P. M. Bell, J. Geophys. Res. **91**, 4673 (1986).

[34] Y. Akahama and H. Kawamura, J. Appl. Phys. **100**, 043516 (2006).

[35] R. J. Angel, J. Gonzalez-Platas, and M. Alvaro, Z. Krist. **229**, 405 (2014).

[36] F. Birch, J. Geophys. Res. **83**, 1257 (1978).

[37] D. Andrault, R. J. Angel, J. L. Mosenfelder, and T. Le Bihan, Am. Miner. **88**, 301 (2003).

[38] D. Andrault, R. G. Tronnes, Z. Konopkova, W. Morgenroth, H. P. Liermann, G. Morard, and M. Mezouar, Am. Mineral. **99**, 2035 (2014).

[39] M. Murakami and J. D. Bass, Phys. Rev. Lett. **104**, 025504 (2010).

[40] S. J. Gaudio, S. Sen, and C. E. Lesher, Geochim. Cosmochim. Ac. **72**, 1222 (2008).

[41] X. Y. Xue, J. F. Stebbins, M. Kanzaki, P. F. McMillan, and B. Poe, Amer. Miner. **76**, 8 (1991).

[42] T. Sato and N. Funamori, Phys. Rev. B **82**, 209604 (2010).

[43] C. Prescher, V. B. Prakapenka, J. Stefanski, S. Jahn, L. B. Skinner, and Y. Wang, Proc. Natl. Acad. Sci. USA. **114**, 10041 (2017).

[44] A. N. Clark, C. E. Lesher, S. D. Jacobsen, and Y. Wang, J. Geophys. Res. **121**, 4232 (2016).

[45] A. N. Clark, C. E. Lesher, S. D. Jacobsen, and S. Sen, Phys. Rev. B **90**, 174110 (2014).

[46] N. de Koker and L. Stixrude, Geophys. J. Int. **183**, 478 (2010).

[47] D. M. Ramo and L. Stixrude, Geophys. Res. Lett. **41**, 4512 (2014).

[48] N. de Koker, B. Karki, and L. Stixrude, Earth Planet. Sci. Lett. **361**, 58 (2013).

[49] C. Liebske and D. J. Frost, Earth Planet. Sci. Lett. **345**, 159 (2012).

[50] A. M. Dziewonski and D. L. Anderson, Phys. Earth Planet. Int. **25**, 297 (1981).

[51] R. Nomura, H. Oszawa, S. Tateno, K. Hirose, J. Hernlund, S. Muto, H. Ishii, and N. Hiraoka, Nature **473**, 199 (2011).

[52] D. Andrault, S. Petitgirard, G. Lo Nigro, J.-L. Devidal, G. Veronesi, G. Garbarino, and M. Mezouar, Nature **487**, 354 (2012).

[53] G. K. Pradhan, G. Fiquet, J. Siebert, A.-L. Auzende, G. Morard, D. Antonangeli, and G. Garbarino, Earth Planet. Sci. Lett. **431**, 247 (2015).

[54] S. Labrosse, J. Hernlund, and N. Coltice, Nature **450**, 866 (2007).

[55] A. Caracausi, G. Avice, P. G. Burnard, E. Furi, and B. Marty, Nature **533**, 82 (2016).

[56] W. Xu, C. Lithgow-Bertelloni, L. Stixrude, and J. Ritsema, Earth Planet. Sci. Lett. **275**, 70 (2008).

Fig. 1. Low-pressure run with a double polished SiO_2 plate immersed in a methanol:ethanol mixture. A-B) Map through the diamonds to determine the path length (x). C-D) Absorption map through the Be gasket (showing three profiles in dark, grey and light grey). E) Correlation between B and D gives the linear absorbance of the sample (colours of the symbols refers to the different correlations with the three different profiles of C).

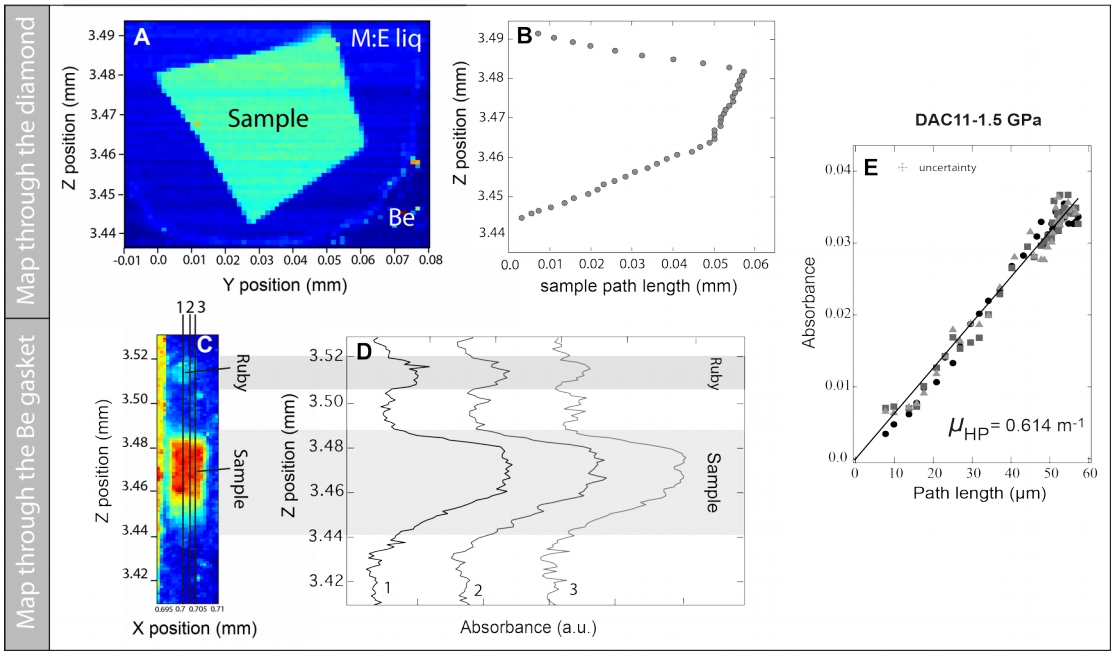

Fig. 2. SiO_2 glass density at high pressure. A) Density measured in this study (one colours per loading) compared to previous experimental [17, 16] and simulation [18] data. B) Strain versus normalized pressure (f-F) plot from the Vinet description [35]. Black lines are guide-to-the-eye. C) Equations of state for the two pressure domains: from 0 to 60 GPa using a second order polynomial; above 60 GPa three EoS are used to fit the data (HP1, HP2 and HP3 see text and Table S2). The black line represents the density of SiO_2 polymorphs [37,38]. The dashed line is the $MgSiO_3$ glass density [30].

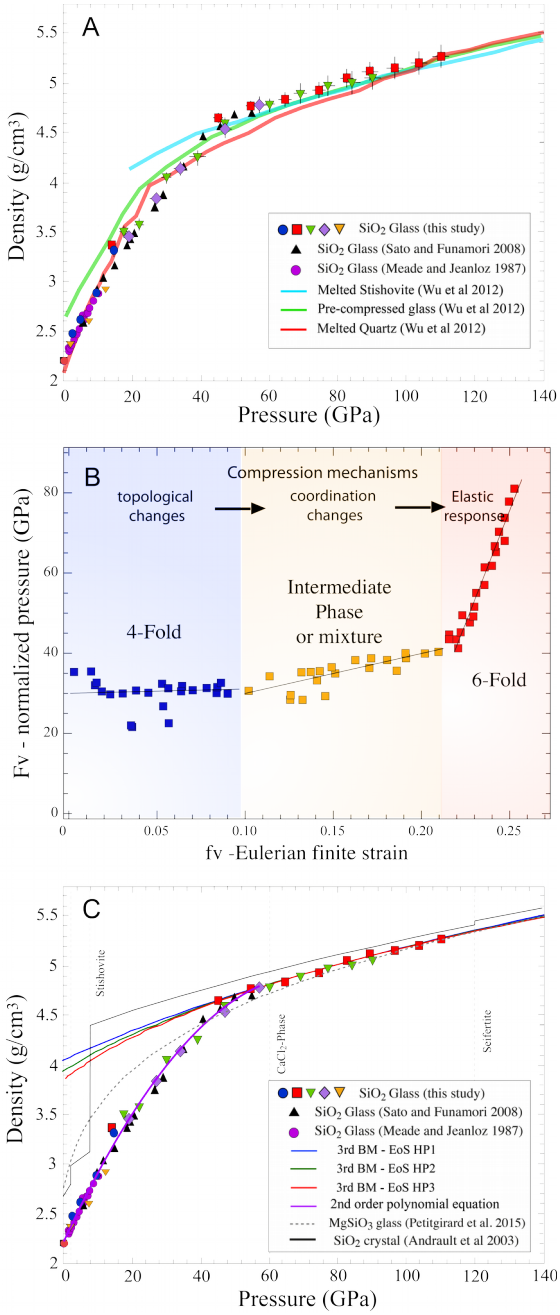

Fig. 3. SiO_2 density at room and high temperature. SiO_2 and $MgSiO_3$ [30] glass density at room temperature in dashed and continuous blue lines respectively. In red densities to lower-mantle temperatures of 4000 K. Density for SiO_2 crystals [37,38], bridgmanite [56] and the PREM-model [50] are plotted for comparison. The red shaded area represents the density at 4000 K with an error of 5 % for possible uncertainties on SiO_2 thermal expansion [46].

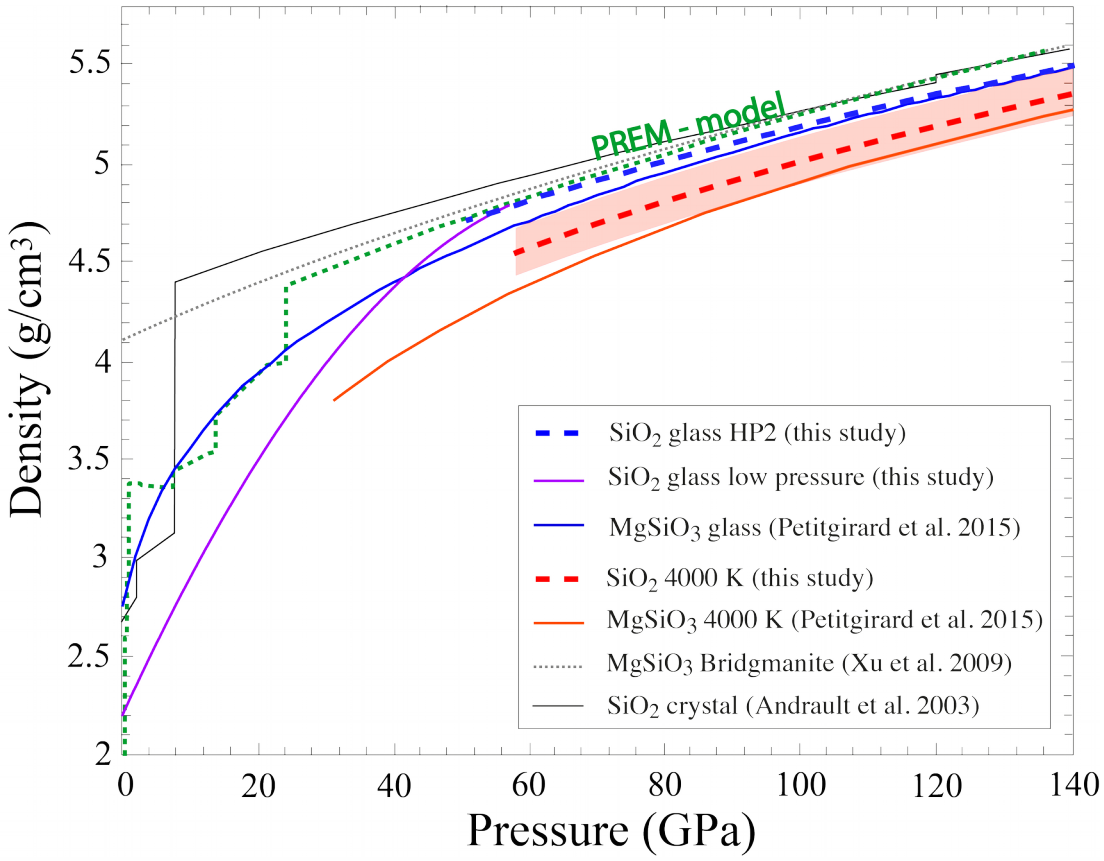
Density (g/cm^3)
Pressure (GPa)
PREM - model
SiO$_2$ glass HP2 (this study)
SiO$_2$ glass low pressure (this study)
MgSiO$_3$ glass (Petitgirard et al. 2015)
SiO$_2$ 4000 K (this study)
MgSiO$_3$ 4000 K (Petitgirard et al. 2015)
MgSiO$_3$ Bridgmanite (Xu et al. 2009)
SiO$_2$ crystal (Andrault et al. 2003)